Improved global wetland carbon isotopic signatures support post-2006 microbial methane emission increase

Youmi Oh, Qianlai Zhuang, Lisa R. Welp, Licheng Liu, Xin Lan, Sourish Basu, Edward J. Dlugokencky, Lori Bruhwiler, John B. Miller, Sylvia E. Michel, et al.

communications earth & environment

ARTICLE

https://doi.org/10.1038/s43247-022-00488-5 OPEN

Improved global wetland carbon isotopic signatures support post-2006 microbial methane emission increase

Youmi Oh[1,2,3✉], Qianlai Zhuang[1,4✉], Lisa R. Welp[1,5], Licheng Liu[1,12], Xin Lan[2,3], Sourish Basu[6,7], Edward J. Dlugokencky[3], Lori Bruhwiler[3], John B. Miller[3], Sylvia E. Michel[8], Stefan Schwietzke[9], Pieter Tans[3], Philippe Ciais[10] & Jeffrey P. Chanton[11]

Atmospheric concentrations of methane, a powerful greenhouse gas, have strongly increased since 2007. Measurements of stable carbon isotopes of methane can constrain emissions if the isotopic compositions are known; however, isotopic compositions of methane emissions from wetlands are poorly constrained despite their importance. Here, we use a process-based biogeochemistry model to calculate the stable carbon isotopic composition of global wetland methane emissions. We estimate a mean global signature of −61.3 ± 0.7‰ and find that tropical wetland emissions are enriched by ~11‰ relative to boreal wetlands. Our model shows improved resolution of regional, latitudinal and global variations in isotopic composition of wetland emissions. Atmospheric simulation scenarios with the improved wetland isotopic composition suggest that increases in atmospheric methane since 2007 are attributable to rising microbial emissions. Our findings substantially reduce uncertainty in the stable carbon isotopic composition of methane emissions from wetlands and improve understanding of the global methane budget.

[1] Department of Earth, Atmospheric, and Planetary Sciences, Purdue University, West Lafayette, IN, USA. [2] Cooperative Institute for Research in Environmental Sciences, University of Colorado, Boulder, CO, USA. [3] Global Monitoring Laboratory, NOAA, Boulder, CO, USA. [4] Department of Agronomy, Purdue University, West Lafayette, IN, USA. [5] Purdue Climate Change Research Center, West Lafayette, IN, USA. [6] Global Modeling and Assimilation Office, NASA Goddard Space Flight Center, Greenbelt, MD, USA. [7] Earth System Science Interdisciplinary Center, University of Maryland, College Park, MD, USA. [8] Institute of Arctic and Alpine Research, University of Colorado, Boulder, CO, USA. [9] Environmental Defense Fund, Berlin, Germany. [10] Laboratoire des Sciences du Climat et de l'Environnement, Gif-sur-Yvette, France. [11] Department of Earth, Ocean, and Atmospheric Sciences, Florida State University, Tallahassee, FL, USA. [12] Present address: Department of Bioproducts and Biosystems Engineering, University of Minnesota, St. Paul, MN, USA. ✉email: youmi.oh@noaa.gov; qzhuang@purdue.edu

Methane (CH_4) is a powerful greenhouse gas, and its atmospheric abundance (in nmol mol^{-1}, abbreviated ppb) has increased by about 170% since the 1750s[1,2]. Unlike the steady increases of atmospheric CO_2 and N_2O, atmospheric CH_4 nearly stabilized from 1998 to 2006 and then rapidly increased with a growth rate averaging ~6 ppb yr^{-1} between 2007 and 2013 and ~11 ppb yr^{-1} between 2014 and 2021. Since 2007, CH_4 has increased while its stable carbon isotopic composition ($\delta^{13}C$-CH_4, Eq. 1) has trended to more negative values, after increasing for 200 years[3–5]. Diagnosing the mechanisms behind these changes continues to generate considerable attention and controversy[6–12].

Measurements of atmospheric CH_4 abundance and $\delta^{13}C$-CH_4, in combination with isotopic signatures of sources and sinks, allow partitioning of CH_4 budgets into different source categories. This is because isotopic signatures of source categories differ substantially, where the $\delta^{13}C$-CH_4 of microbial sources (mean of −61.7 with variability of 6.2‰) is isotopically more depleted than fossil (mean of −44.8 with variability of 10.7‰) and biomass burning (mean of −26.2 with variability of 4.8‰) sources[9,13]. The destruction of CH_4, primarily by reaction with hydroxyl radical (OH), isotopically enriches atmospheric CH_4 relative to the emission-weighted source signature[7,14,15]. Due to a wide range of $\delta^{13}C$-CH_4 in each source category[13], spatial and temporal distributions must be known to reduce the uncertainty in source partitioning. Wetlands are the largest single natural CH_4 source and strongly influence atmospheric $\delta^{13}C$-CH_4 changes[12], but the spatial and temporal information of wetland $\delta^{13}C$-CH_4 is limited, and often a single uniform value is assumed[15,16]. Studies show that source partitioning in atmospheric modeling is highly sensitive to spatiotemporal understanding of wetland $\delta^{13}C$-CH_4[9].

Observations of global wetland $\delta^{13}C$-CH_4 show that CH_4 emitted from boreal wetlands is isotopically more depleted than CH_4 emitted from the tropics[17–19]; proposed causes include the abundance of C_4 plants influencing the $\delta^{13}C$ of precursor organic matter (POM) ($\delta^{13}C$-POM), differences in CH_4-producing archaea (methanogen) communities, and different CH_4 transport processes[18,20–22]. Ganesan et al.[23] produced a spatially-resolved global wetland $\delta^{13}C$-CH_4 distribution, but their study did not simulate temporal variability and did not fully represent fractionation processes that change based on meteorology, soil and vegetation properties.

Here, we incorporate a carbon isotope module into a biogeochemistry model, the Terrestrial Ecosystem Model (TEM)[24,25] to simulate and mechanistically understand the global wetland $\delta^{13}C$-CH_4 distribution. The model is evaluated using site-level and regional observations. We then use this model to understand the mechanisms behind the spatial and temporal variability of wetland $\delta^{13}C$-CH_4, and conduct uncertainty and sensitivity tests. Finally, we investigate the effect of new wetland isotope maps on atmospheric $\delta^{13}C$-CH_4 and global CH_4 emissions by using an atmospheric model and atmospheric observations[5,26].

Results

Modeling wetland $\delta^{13}C$-CH_4 dynamics. TEM simulates CH_4 production, oxidation, and transport between soils and the atmosphere (Eqs. 3–10)[24,25,27,28]. A carbon isotope-enabled module is incorporated into TEM, referred to as isoTEM, which explicitly considers carbon isotopic fractionation processes in wetlands (Fig. 1). The isotopic fractionation factor (α) for each process is defined in Eq. 2[20], where α is larger than 1 when the product is isotopically more depleted than the reactant.

$\delta^{13}C$-POM is determined by the global C_3 and C_4 plant distribution (Supplementary Fig. 1)[29], where C_4 vegetation is isotopically enriched due to its photosynthetic pathway[30]. We incorporated observed long-term trends of atmospheric $\delta^{13}C$-CO_2 into soil $\delta^{13}C$-POM (Supplementary Fig. 2)[31–33]. CH_4 is produced from POM in anaerobic soils by two distinct methanogen communities: hydrogenotrophic methanogens (HMs) which use H_2 and CO_2 and acetoclastic methanogens (AMs) which use acetate[34]. The fractional contribution of these pathways is important because HMs produce isotopically more depleted CH_4 compared to AMs (α_{HM} and α_{AM} in Eq. 12)[19,35]. To quantify the fractional contribution, we used in situ observations from Holmes et al.[19] and conducted a regression analysis between the fractional contribution and main environmental factors, including soil pH, carbon, and latitude (Eq. 11, Supplementary Fig. 3, and Supplementary Table 1). Total produced $\delta^{13}C$-CH_4 is then calculated using a mixing of CH_4 pools from the two methanogen communities (Eqs. 13–14). The CH_4 produced is partly oxidized by methanotrophs in aerobic soil layers[36] with $^{12}CH_4$ being oxidized preferentially relative to $^{13}CH_4$ (α_{MO} in Eq. 15). Then, the remaining CH_4 is emitted to the atmosphere through three processes: plant-mediated transport, diffusion, and ebullition, with fractionation factors of α_{TP}, α_{TD}, and α_{TE}, respectively (Eq. 16)[20]. We calculated oxidized and emitted $\delta^{13}C$-CH_4 using the ratio of oxidation and transport processes and their fractionation factors (Eqs. 17–22) (Method "Model development").

We optimized four fractionation factors related to CH_4 production, oxidation, and plant-mediated transport (α_{HM}, α_{AM}, α_{MO}, α_{TP}) using field observations in boreal (50–90°N), temperate (30–50°N/S), and tropical (<30°N/S) wetlands[35,37,38] (Eqs. 12, 15, 16, Supplementary Table 2–4 and Supplementary Figs. 4, 5). We

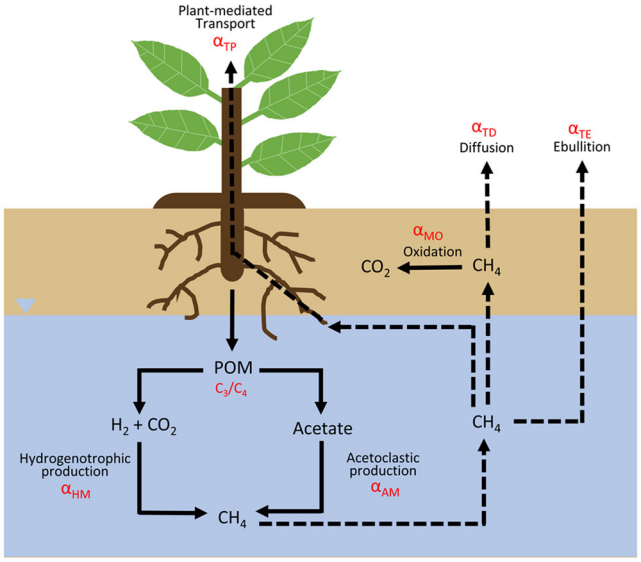

Fig. 1 Schematic diagram of wetland CH_4 dynamics and fractionations for isoTEM. The model simulates $\delta^{13}C$ of precursor organic matter (POM) ($\delta^{13}C$-POM), CH_4 production, oxidation, and transport to the surface. $\delta^{13}C$-POM is determined by global C_3/C_4 plant distribution and long-term trends of atmospheric $\delta^{13}C$-CO_2. CH_4 is produced by two pathways, one using H_2 and CO_2 and another using acetate, with fractionation factors (α) for HMs (α_{HM}) ≈ 1.030–1.080 and for AMs (α_{AM}) ≈ 1.000–1.040. Produced CH_4 is partly oxidized by methanotrophs with a fractionation factor α_{MO} ≈ 1.015–1.035. Residual produced CH_4 is emitted to the surface via three processes, plant-mediated transport (TP), diffusion (TD), and ebullition (TE), with different fractionations, α_{TP} ≈ 1.000–1.030, α_{TD} ≈ 1.005, α_{TE} ≈ 1.000, respectively (Supplementary Tables 2–4 and Method "Model development, Model optimization"). Bold and dashed lines in the figure refer to chemical and transport processes, respectively.

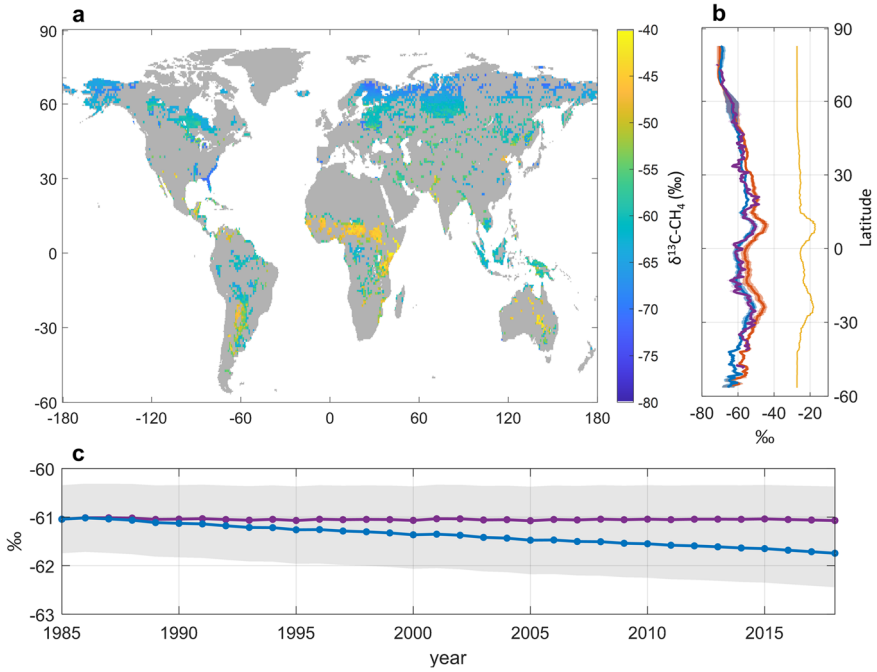

Fig. 2 Global distribution of wetland δ^{13}C-CH$_4$ and its latitudinal and long-term gradients simulated by isoTEM. a Modeled global wetland δ^{13}C-CH$_4$ for wetland grid cells with static inundation data[49]. **b** Mean latitudinal distribution of δ^{13}C of POM (yellow), produced CH$_4$ (red), and CH$_4$ emitted to the atmosphere for all grid cells (blue) and flux-weighted grid cells (purple). **c** Long-term trends of global mean wetland δ^{13}C-CH$_4$ with and without incorporating long-term trend in δ^{13}C-POM (blue and purple, respectively). The shaded area in (**b**, **c**) represents one standard deviation determined from 20 ensembles of simulations where the optimized parameters were varied.

set α_{TE} to 1.000 and α_{TD} to 1.005 based on previous studies[20] since ebullition and diffusion are governed by physical processes. To quantify uncertainties in model simulations, we used 20 ensemble members of optimization. We simulated global wetland CH$_4$ fluxes and their isotopic signatures during 1984–2016 at a spatial resolution of 0.5° with a 50-year spin-up to let δ^{13}C-CH$_4$ of carbon pools come to a steady state (Methods "Model optimization, Simulation setup").

Simulated wetland δ^{13}C-CH$_4$ and its comparison with observations. We estimated the mean global wetland source signature to be −61.3 ± 0.7‰ during 1984–2016 (Fig. 2a). This value is more enriched than the mean wetland signature of −62.3‰ in Ganesan et al.[23] but similar to the mean value of −61.5‰ reported in Sherwood et al.[13] (Supplementary Figs. 8, 9). The latitudinal distribution of δ^{13}C-CH$_4$ ranges from a mean of −57 ± 3‰ in the tropics to −68 ± 4‰ in boreal regions (Fig. 2b). Our model simulates isotopically depleted global δ^{13}C-CH$_4$ during the summer due to larger emissions from boreal regions (Supplementary Fig. 10) and a long-term trend of −0.7 ± 0.1‰ during 1984–2016 (blue line in Fig. 2c) when incorporating the long-term trend in δ^{13}C-POM (Supplementary Fig. 2)

We compared the magnitude and spatial variability of the simulated wetland δ^{13}C-CH$_4$ with site-level observations (Method "Model-data comparison"). We used 70 in situ measurements of global wetland δ^{13}C-CH$_4$ from previous studies after excluding the measurements applied for optimization (Supplementary Data 1, Supplementary Fig. 11)[13,19]. We showed that isoTEM reduced the root mean square error (RMSE) by 40% compared to Ganesan et al.[23] (2.2 vs. 3.6) (Fig. 3a, b). Compared to a static isoTEM map in July, 2016, temporally-varying isoTEM reduced the RMSE slightly (2.2 vs. 2.4) (Supplementary Fig. 12). Ganesan et al.[23] prescribed maximum and minimum values as boundary conditions, resulting in unrealistic clusters of wetland δ^{13}C-CH$_4$ near −65‰ for boreal and −60‰ for tropical sites (Fig. 3a and Supplementary Fig. 9).

Furthermore, we compared the spatial variability of simulated wetland δ^{13}C-CH$_4$ with estimated signatures from airborne measurements for three regions in Alaska during 2012-2013 and 2015 using Miller-Tans plots (Fig. 3c–e) (Method "Model data comparison")[39]. In situ flux observations collected across Alaskan wetlands show an average of −65‰, but with a large 9‰ variance[40], which could be due to changes in wetland habitat including soil nutrients, pH, and vegetation distribution. The estimated signatures from observation also show that compared with δ^{13}C-CH$_4$ from the North Slope of Alaska (−65 ± 1‰), δ^{13}C-CH$_4$ from interior Alaska is more depleted (−69 ± 6) and δ^{13}C-CH$_4$ from southwest Alaska is more enriched (−59 ± 4‰) (Supplementary Fig. 13 and Supplementary Table 5). IsoTEM reproduces the spatial variability (−67 ± 1, −68 ± 1, and −61 ± 2‰ for North Slope, interior, and southwest Alaska, respectively), whereas Ganesan et al.[23] simulated no spatial variability around −65‰ (Fig. 3e). IsoTEM simulates the spatial variability as the model optimized parameters for vegetated and non-vegetated sites separately and incorporated meteorology and soil inputs that vary spatially and temporally.

Mechanistic understanding of spatial and temporal variability of wetland δ^{13}C-CH$_4$. We investigated the relative importance of the isotopic fractionation processes that affect the latitudinal gradient of wetland δ^{13}C-CH$_4$ (Fig. 2b and Supplementary Fig. 14). First, compared to the boreal zone, δ^{13}C-POM is enriched in the tropics by 5 ± 2‰ as C$_4$ plants are more prevalent (yellow line in Fig. 2b, Supplementary Figs. 1, 14a). Second, due to a larger fraction of AM in the tropics (Supplementary Fig. 3), the δ^{13}C-CH$_4$ produced by methanogens is enriched by 12 ± 3‰ (red line in Fig. 2b, Supplementary Fig. 14b). Third, δ^{13}C-CH$_4$ emitted from wetlands is 6 ± 4‰ more depleted in the tropics due to a larger proportion of plant-mediated transport causing higher

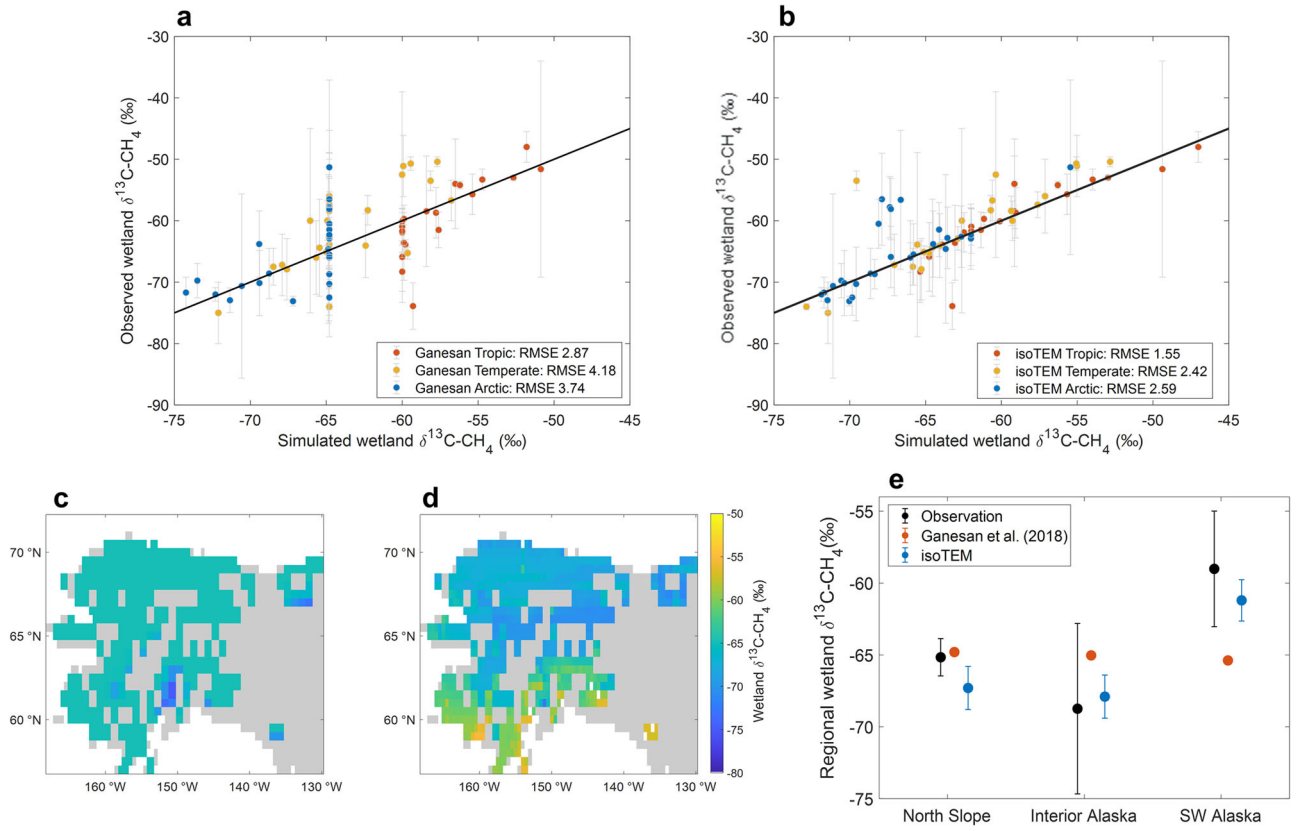

Fig. 3 Site-level and regional model-data comparison of wetland δ^{13}C-CH$_4$. a, **b** Site-level model-data comparison of observations with (**a**) Ganesan et al.[23] and (**b**) temporally-varying isoTEM. **c**–**e** Regional model-data comparison of simulated wetland δ^{13}C-CH$_4$ in Alaska by (**c**) Ganesan et al.[23] and (**d**) isoTEM, and (**e**) their comparison with observation-based source signatures from NOAA aircraft measurements. The source signature is derived using Miller-Tans plots[39]. All observation data used for site-level comparison are listed in Supplementary Data 1. Error bars for observations in (**a**, **b**, **e**) represent one standard deviation of measured/inferred wetland δ^{13}C-CH$_4$. Error bars for isoTEM in panel e represent one standard deviation determined from 20 ensemble simulations where the optimized parameters were varied.

effective transport fractionation (α_T) (blue line in Fig. 2b, Eq. 19, Supplementary Figs. 14d, 15, 16). Thus, in our simulation, δ^{13}C-CH$_4$ emitted from tropical wetlands is enriched by ~11‰ compared to boreal wetlands. This difference is strengthened due to the distribution of C$_4$ plants (+5 ± 2‰) and the fractional contribution of differing methanogen communities (+12 ± 3‰) but weakened due to plant-mediated transport (−6 ± 4‰).

The long-term decrease in wetland δ^{13}C-CH$_4$ simulated by isoTEM is mostly due to the decrease in atmospheric δ^{13}C-CO$_2$[32]. The decreasing trend is incorporated into δ^{13}C-POM (Supplementary Fig. 2) and causes the long-term decrease in wetland δ^{13}C-CH$_4$ of ~0.7‰ from 1984 to 2016 (blue line in Fig. 2c)[31]. We conducted a simulation without the decreasing trend in δ^{13}C-POM, which showed that increased temperature caused plant productivity and plant-mediated transport to increase and δ^{13}C-CH$_4$ to decrease by ~0.1‰ during 1984–2016 (purple line in Fig. 2c and Supplementary Fig. 15). This implies that wetland δ^{13}C-CH$_4$ could further change in the future due to decreases in δ^{13}C-POM and increases in plant-mediated transport.

There is no continuous long-term measurements of wetland δ^{13}C-CH$_4$ to verify our simulated long-term trend. Instead, we ran a regression analysis using observations collected from various wetland locations since the early 1980s (Supplementary Data 1) (Method "Uncertainty and sensitivity tests"). The results show that the representation of data increases when adding year as a parameter for the regression analysis (Supplementary Table 6), and the observed data show a long-term decreasing trend with year (~−0.1‰ year^{-1}) (Supplementary Fig. 17). More continuous long-term observations of wetland δ^{13}C-CH$_4$ are necessary to further verify the simulated long-term trends in wetland δ^{13}C-CH$_4$.

Uncertainty and sensitivity tests. The version of TEM that we use for this study explicitly simulates soil CO$_2$ and CH$_4$ but not soil H$_2$ and acetate pools[27], because the spatial and temporal soil H$_2$ and acetate pools are highly uncertain, and it is hard to verify the simulated pool changes with limited observations. On the contrary, the CH$_4$ production, oxidation, and transport processes in TEM have been thoroughly validated for global regions from previous studies[24,25,27,41–44]. Therefore, instead of introducing additional uncertainty from explicitly simulating H$_2$ and acetate pools that cannot be validated, we applied the observed fraction of different methanogen communities (f_{HM}) based on regression to the total CH$_4$ production rates simulated by TEM (Supplementary Fig. 3 and Supplementary Table 1). Thus, in our simulation, the fraction of HM and AM (f_{HM}) changes spatially but not temporally.

To quantify the uncertainty of our regression analysis of f_{HM}, we ran additional sensitivity tests by varying the f_{HM} based on the uncertainty from Markov Chain Monte Carlo approach (Method "Uncertainty and sensitivity tests" and Supplementary Table 1)[45]. The results show that varying the parameters do not change the wetland δ^{13}C-CH$_4$ substantially (<1%) (Supplementary Table 7). We acknowledge that this simplification would cause uncertainty in our model results, and future studies should explicitly measure

changes in H_2 and acetate concentrations in soils to incorporate the detailed processes into the model.

The simplification of CH_4 production processes may also cause uncertainty in the fractionation as we do not explicitly simulate fractionation processes from POM to CO_2/acetate and from CO_2/acetate to CH_4. However, studies show that fractionation factors of the fermentation (POM to CO_2) and syntrophy (POM to acetate) processes are minor ($\alpha \approx 1.00$)[19,46,47]. There may be additional CO_2 produced by acetoclastic methanogenesis that have large fractionation ($\alpha \approx 1.05$), but the fraction is negligible from observations[19]. Thus, we believe our fractionation factors for HMs and AMs (α_{HM} and α_{AM}, respectively) reasonably represent the major fractionation processes of CH_4 production.

Furthermore, to quantify the influence of the uncertainty of our model inputs on simulation results, we varied temperature, precipitation, net primary productivity (NPP), atmospheric CH_4, and applied transient inundation maps[48] (Method "Uncertainty and sensitivity tests"). The results show that meteorology and substrate inputs alter mean wetland $\delta^{13}C\text{-}CH_4$ by ±1‰ (Supplementary Table 7). Our TEM simulations showed that CH_4 fluxes are sensitive to these inputs[27]. However, $\delta^{13}C\text{-}CH_4$ shows small changes because the fractionation is determined by the fraction of CH_4 oxidation and transport processes (Eqs. 21, 22), that are calculated as a function of soil CH_4 production and the resultant CH_4 concentration changes (C_M in Eqs. 6–10). When CH_4 production increases due to input changes, CH_4 oxidation and transport increase simultaneously, causing minor variation in the fraction of oxidation and transport (Supplementary Fig. 16). Inundation datasets also alter wetland $\delta^{13}C\text{-}CH_4$ by changing the areas where wetland emissions occur (±2‰) (Supplementary Table 7 and Supplementary Figs. 6, 7).

Implication for atmospheric modeling and global CH_4 budget. We constructed four scenarios with different wetland emissions and isotopic signature maps as inputs for TM5 atmospheric modeling during 1984–2016 to understand the impacts of spatially- and temporally-resolved wetland $\delta^{13}C\text{-}CH_4$ (Table 1). Scenario A uses a globally uniform value of wetland $\delta^{13}C\text{-}CH_4$; Scenario B uses a temporally static but spatially variable wetland isotope map from Ganesan et al.[23]; and Scenario C uses spatially- and temporally-resolved maps from isoTEM. We used the same wetland fluxes[27] with a static inundation map[49] for Scenarios A–C that applied a step increase in fluxes in 2007 and 2014 by hypothesizing that microbial wetland emissions are the dominant driver of the post-2006 atmospheric CH_4 increase[9,26,50] (46 $Tgyr^{-1}$ increase in total 2016 emissions across the global wetlands compared to the averaged total emissions in 1999–2006) (Supplementary Fig. 19). However, since other studies have suggested an increase in fossil emission as a dominant driver for post-2006 CH_4 increases[12], we created scenario D that uses isoTEM wetland isotope maps with increases in both microbial and fossil emissions since 2007 (Table 1).

For Scenarios A–D, we adjusted global mean fossil and ruminant fluxes simultaneously to satisfy the long-term average mass balance of atmospheric CH_4 (Fig. 4a) and $\delta^{13}C\text{-}CH_4$ (Method "Forward modeling using TM5 atmospheric model"), as done by Lan et al.[26]. These adjustments bring the long-term global average $\delta^{13}C\text{-}CH_4$ from simulation to the observed atmospheric levels without changing the post-2006 trends in simulated $\delta^{13}C\text{-}CH_4$[9,26]. After adjustments, global mean fossil fluxes in scenarios A–D are between 170 and 190 $Tgyr^{-1}$ (Supplementary Fig. 19),within the uncertainty range in Schwietzke et al.[9]. For all other fluxes, their isotopic signatures, and CH_4 sinks that include OH, Cl, and $O(^1D)$[14,51,52], we used the same setup in our model as in Lan et al.[26] (Supplementary Table 8). We compared simulated CH_4 and $\delta^{13}C\text{-}CH_4$ with observations from NOAA/INSTAAR global flask-air measurements (Supplementary Table 10)[2,5].

The atmospheric simulation showed that Scenarios A–C follow the observed $\delta^{13}C\text{-}CH_4$ trend reasonably closely (Fig. 4b). However, Scenario D, which hypothesizes a post-2006 increase in microbial and fossil fluxes, does not follow the decreasing trend in global mean $\delta^{13}C\text{-}CH_4$. As pointed out earlier[8,9,26,50], the magnitude of the $\delta^{13}C\text{-}CH_4$ decrease suggests that the increase in microbial emissions dominates fossil emissions in the post-2006 global CH_4 increase. We also confirmed a dominant increase in post-2006 microbial emissions, even though the long-term decrease in wetland $\delta^{13}C\text{-}CH_4$ of ~0.7‰ allow for a larger fossil emission increase. An additional simulation of Scenario C without including the long-term decrease in wetland $\delta^{13}C\text{-}CH_4$ shows differences of ~0.1‰ in simulated atmospheric $\delta^{13}C\text{-}CH_4$ in 2016 compared with model results with long-term wetland $\delta^{13}C\text{-}CH_4$ trend (Supplementary Fig. 23). This difference can accommodate more post-2006 emission increases from isotopically enriched fossil sources for Scenario C.

We differentiated Scenarios A–C by comparing their simulated latitudinal gradients of atmospheric $\delta^{13}C\text{-}CH_4$ with observations (Fig. 4c and Supplementary Fig. 20). The observed mean latitudinal gradient during 1998–2016 shows more negative $\delta^{13}C\text{-}CH_4$ at northern high latitudes compared to the Southern Hemisphere by 0.45 ± 0.05‰ (Supplementary Table 9), resulting from the dominance of northern emissions combined with the subsequent fractionation by reaction with OH during transport to the Southern Hemisphere[17]. Scenario C, which uses IsoTEM maps,

Table 1 Setup of TM5 atmospheric modeling for Scenarios A–D.

Scenario	Wetland isotope map	Assumption of post-2006 CH_4 increase	Global mass balance of CH_4 and $\delta^{13}C\text{-}CH_4$[a]
A: Uniform w/Microbial Increase	One uniform value (−62.3‰, a mean signature of Ganesan et al.[23])	Wetland emission increase (46 $TgCH_4yr^{-1}$ increase from 1999–2006 to 2016)	Yes
B: Ganesan w/Microbial Increase	One spatial map from Ganesan et al.[23] (mean of −62.3‰)		
C: isoTEM w/Microbial Increase	Spatio-temporally-resolved maps from isoTEM (mean of −61.3‰) (this study)		
D: isoTEM w/ Microbial + Fossil Increase		Wetland (60%) + fossil (40%) emission increase[12] (28 $TgCH_4yr^{-1}$ increase from wetland, 18 $TgCH_4yr^{-1}$ increase from fossil, from 1999–2006 to 2016)	

[a]Using a global mass balance model from previous studies[9,26], the long-term mean fossil and ruminant fluxes were adjusted from EDGAR 4.3.2 inventory to match the observed atmospheric growth rate of CH_4 during 1984–2016 and the 1998–2016 mean of $\delta^{13}C\text{-}CH_4$. By conducting the mass balance for all scenarios, we intended to reduce the spin-up time for atmospheric $\delta^{13}C\text{-}CH_4$ to be stabilized and compare all scenarios fairly (Method "Forward modeling using TM5 atmospheric model").

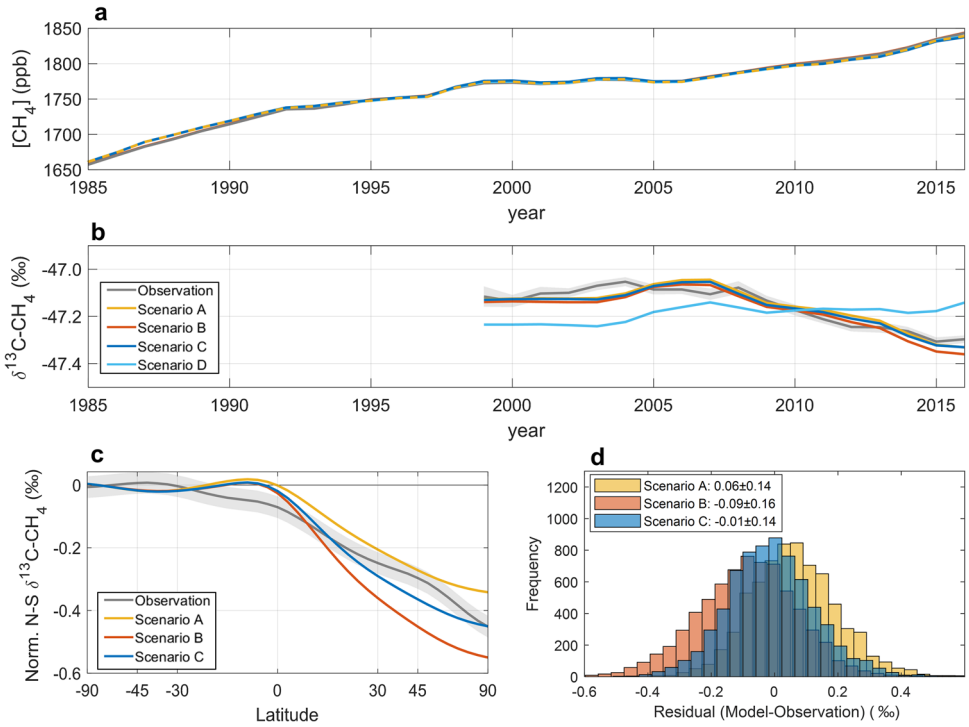

Fig. 4 Observed and simulated atmospheric CH_4 and $\delta^{13}C$-CH_4 from TM5 atmospheric modeling. a, **b** Model-data comparison of long-term trend of (**a**) atmospheric CH_4 from 1985 to 2016 (in ppb) and (**b**) $\delta^{13}C$-CH_4 from 1999 to 2016 (in ‰) by observation (gray) and simulations from Scenario A (yellow), B (red), C (blue), and D (skyblue). **c** Model-data comparison of normalized north–south gradient of atmospheric $\delta^{13}C$-CH_4 for Scenario A (yellow), B (red), and C (blue) in 2012. The north–south $\delta^{13}C$-CH_4 was calculated by zonally-averaging the surface $\delta^{13}C$-CH_4 and normalized based on the mean $\delta^{13}C$-CH_4 at 60–90 °S. The normalized north–south $\delta^{13}C$-CH_4 for other years is in Supplementary Fig. 20 and Supplementary Table 9. **d** Histogram of the difference between simulated and observed $\delta^{13}C$-CH_4 for Scenario A (yellow), B (red), and C (blue) for 6 measurement sites located in the northern hemisphere. The histogram plots for all measurement sites are in Supplementary Fig. 22. Information about Scenarios A–D is in Table 1.

best reproduces the observed north–south gradient (0.48‰); Scenarios A and B under- and over-estimate the gradient by ~0.1‰ (0.37‰, and 0.59‰, respectively). The difference is also clear when comparing simulated atmospheric $\delta^{13}C$-CH_4 of Scenarios A–C at 10 measurement sites (Supplementary Figs. 21, 22 and Supplementary Table 10). The simulated and observed atmospheric $\delta^{13}C$-CH_4 differ the most at Northern Hemispheric sites, where Scenario C best reproduces the atmospheric $\delta^{13}C$-CH_4 data, but Scenario A and Scenario B simulate more negative and positive $\delta^{13}C$-CH_4, respectively (Fig. 4d).

The difference in north–south gradient of atmospheric $\delta^{13}C$-CH_4 between scenarios in Fig. 4c has an implication on regional partitioning of sources. Our sensitivity test of atmospheric modeling showed that all scenarios with transient inundation data[48] (Scenarios E–G) underestimated the north–south $\delta^{13}C$-CH_4 gradient (0.27 ± 0.06‰) compared with observations (0.45 ± 0.05‰) (Method "Forward modeling using TM5 atmospheric model", Supplementary Table 11, Supplementary Figs. 26–30). Thus, we ran an additional Scenario H that increased emissions from boreal wetlands by 2.5 times over the original transient data (Supplementary Fig. 26 and Supplementary Table 11), which increased the north–south gradient by ~0.1‰ and improved the match with the observed north–south $\delta^{13}C$-CH_4 gradient (0.39‰) (Supplementary Figs. 29, 30).

Discussion

The atmospheric CH_4 burden has grown rapidly since 2007, and the largest annual increase since NOAA began measurements in 1983 was observed in 2021[53,54]. Since 2019, $\delta^{13}C$-CH_4 decreased more steeply[55], suggesting a further increase in microbial emissions as this and other studies suggest[8,9,26,50]. The microbial sources include anthropogenic emissions from ruminants, agriculture, and waste, and natural emissions from wetlands and other aquatic ecosystems[12]. Our simulation with increase in wetland emissions can reproduce the observed post-2006 $\delta^{13}C$-CH_4 decrease (Fig. 4), and our additional sensitivity test with increase in anthropogenic microbial emissions also tracks the post-2006 $\delta^{13}C$-CH_4 decrease (Supplementary Figs. 24, 25). However, the scenario with emission increase from both microbial and fossil sources did not reproduce the decreasing trend in atmospheric $\delta^{13}C$-CH_4 (Scenario D in Fig. 4). Other atmospheric studies that use atmospheric $\delta^{13}C$-CH_4 observations also showed that fossil emission increase is not a dominant reason of recent CH_4 increase[26,56].

Atmospheric $\delta^{13}C$-CH_4 measurements have not been widely used to inform global methane budget because of uncertainty and spatiotemporal variation in source signatures, specifically citing limitation in wetland source signatures[11]. In this study, we mechanistically explain the spatiotemporal variations of wetland $\delta^{13}C$-CH_4 and validate the simulation using regional, latitudinal, and global measurements, which substantially reduce the uncertainty in $\delta^{13}C$-CH_4 source signatures (Fig. 3). The small decreasing trend in wetland $\delta^{13}C$-CH_4 allow for more fossil emission increase in our estimate, but cannot change the conclusion that fossil emission increases are not the dominant driver for post-2006 global CH_4 increases.

This study considers wetland $\delta^{13}C$-CH_4 during the historical period only, but the future changes in wetland $\delta^{13}C$-CH_4 will depend on multiple factors. First, our simulation shows that changes in $\delta^{13}C$-POM affect wetland $\delta^{13}C$-CH_4 as SOC is mostly derived from new carbon from vegetation. The simulated active layer depth from a previous study[57] shows that the active layer

depth had a minor change during our simulation period (mean of <0.1 m) (Supplementary Fig. 18). However, the usage of old stored carbon in Arctic permafrost may play an important role as a substrate for methanogens in the future[58]. Also, studies found the importance of microbial fossil CH_4 emissions from Arctic regions in the future[59,60]. The emissions are partially included as geologic seep emissions in our atmospheric modeling simulation (Supplementary Fig. 19 and Supplementary Table 8), and we also considered microbial fossil emissions with depleted δ^{13}C-CH_4 in our total fossil emission estimates[26]. Lastly, our simulation shows that the increase in NPP cause more plant-mediated transport. This effect will be more important in the future as plant functional types and plant growth change due to temperature increase.

There are several aspects of the model that could be improved. First, our optimization of fractionation factors was based on limited observations; additional long-term measurements of wetland δ^{13}C-CH_4 would reduce the uncertainty. Second, the fractional contribution of two methanogen communities (HMs and AMs) changes spatially but not temporally in the model. We need a better understanding of temporal changes in methanogen communities especially following permafrost thaw and disturbance[35], and explicitly measure changes in H_2 and acetate concentrations in soils to incorporate detailed CH_4 production processes into the model. Third, various vertical methanogenic and non-methanogenic processes change δ^{13}C of CH_4 and CO_2, the vertical CO_2/CH_4 ratios, and thus δ^{13}C-CH_4 emitted from wetlands, since CO_2 is a substrate for HM[61,62]. We need to identify detailed vertical subsurface processes by conducting manipulation experiments using isotopic labeling analysis and inhibitor techniques to include those fractionation processes in future modeling studies[63]. Fourth, current wetland models do not simulate large CH_4 emissions and δ^{13}C-CH_4 from tropical tree stems and aquatic sources properly[64–66]. More measurements from these sources are crucial to improve the estimate of natural CH_4 emission and δ^{13}C-CH_4 changes.

Conclusion

To the best of our knowledge, this study is the first to use a biogeochemistry model to mechanistically explain and reduce the uncertainty in global wetland δ^{13}C-CH_4. IsoTEM explains the latitudinal gradient of wetland δ^{13}C-CH_4 that is increased by the distribution of C_3/C_4 plants and methanogen community type but decreased by plant-mediated transport. The long-term trends of the simulated wetland δ^{13}C-CH_4 is controlled by δ^{13}C-POM and plant-mediated transport. Our results suggest that rising microbial emissions is the dominant driver for the post-2006 global CH_4 increase and the concurrent decrease in atmospheric δ^{13}C-CH_4, and the isoTEM spatial distribution of wetland δ^{13}C-CH_4 better reproduces the observed atmospheric δ^{13}C-CH_4 latitudinal gradient.

Methods

Model development. We incorporated a carbon isotope module of methane (CH_4) into an existing process-based biogeochemistry model, the TEM (Fig. 1). The stable carbon isotope in delta notation (δ) describes the ratio of the heavy isotope to the light isotope in the sample ($R_{sam} = (^{13}C/^{12}C)_{sam}$) relative to a known standard ratio, R_{std}, which is Vienna Pee Dee Belemnite (VPDB) for carbon[20] (Eq. 1). The deviation of this ratio-of-ratios from one is multiplied by 1000 to express isotope variations in parts per thousand (‰, permil). To express isotopic fractionation for the reaction A → B, we used a fractionation factor (α) defined in Eq. 2[20], where reactant A is in the numerator and product B is in the denominator. If α is larger than 1, the δ^{13}C of product is isotopically more depleted in the heavy isotope than the δ^{13}C of reactant, and if α is smaller than 1, the δ^{13}C of product is more enriched in ^{13}C than the δ^{13}C of reactant.

$$\delta^{13}C = (R_{sam}/R_{std}) - 1 \quad (1)$$

$$\alpha = \frac{R_A}{R_B} = \left(\frac{\delta^{13}C_A}{1000} + 1\right) \Big/ \left(\frac{\delta^{13}C_B}{1000} + 1\right) \quad (2)$$

Terrestrial Ecosystem Model (TEM). TEM is a commonly used biogeochemistry model and its CH_4, soil, thermal, and hydrological dynamics have been evaluated in previous studies[24,28,41–44]. The CH_4 dynamics module of TEM simulates CH_4 production, oxidation, and three transport processes—diffusion, ebullition, and plant-mediated transport—between soil and atmosphere. Please refer to the details of TEM in Oh et al.[25] and Liu et al.[27].

In TEM wetland model, changes in CH_4 concentrations (C_M) at depth z and time t ($\partial C_M(z,t)/\partial t$) are governed by Eq. 3, where $M_p(z,t)$, $M_o(z,t)$, $R_p(z,t)$, and $R_E(z,t)$ are CH_4 production, oxidation, plant-mediated transport, and ebullition rates, respectively, and $\partial F_D(z,t)/\partial z$ represents flux divergence from gaseous and aqueous diffusion. CH_4 is produced by methanogens in anaerobic soils (M_P) and is calculated by multiplying maximum potential production rate (M_{GO}) and limiting functions of substrate, soil temperature, pH, and redox potentials (S_{OM}, M_{ST}, pH, and Rx, respectively) (Eq. 4). For this study, we assume that substrates for methanogens are mainly from soil organic carbon (SOC) derived from vegetation (Net Primary Productivity, NPP), where $NPP(mon)$ is monthly NPP (gC m^{-2} month^{-1}), NPP_{MAX} is ecosystem-specific maximum monthly NPP, and $f(C_{DIS}(z))$ describes the relative availability of organic carbon substrate at depth z (Eq. 5). The substrate availability changes depending on atmospheric CO_2, meteorology, and soil properties[67].

$$\frac{\partial C_M(z,t)}{\partial t} = M_P(z,t) - M_O(z,t) - \frac{\partial F_D(z,t)}{\partial z} - R_P(z,t) - R_E(z,t) \quad (3)$$

$$M_{P,TEM}(z,t) = M_{G0} f(S_{OM}(z,t)) f(M_{ST}(z,t)) f(pH(z,t)) f(R_x(z,t)) \quad (4)$$

$$f(S_{OM}(z,t)) = \left(1 + \frac{NPP(mon)}{NPP_{\max}}\right) f(C_{DIS}(z)) \quad (5)$$

The produced CH_4 is partly oxidized by methanotrophs and is calculated by the multiplying the maximum potential oxidation rate (O_{MAX}) and limiting functions of CH_4 concentration, soil temperature, soil moisture, redox potential, nitrogen deposition, diffusion limited by high soil moisture, and oxygen concentration (C_M, T_{SOIL}, E_{SM}, R_{OX}, N_{DP}, D_{MS}, and C_{O2} respectively) (Eq. 6). We use Michaelis-Menten kinetics with $k_{CH4,LAM}$ of 5 μM for the CH_4 limitation (Eq. 7).

$$M_{O,TEM}(z,t) = O_{MAX} f(C_M(z,t)) f(T_{SOIL}(z,t)) f(E_{SM}(z,t)) F(R_{OX}(z,t)) f(N_{dp}(z,t)) f(D_{ms}(z,t)) f(C_{O_2}(z)) \quad (6)$$

$$f(C_M(z,t)) = \frac{C_M(z,t)}{k_{CH4,LAM} + C_M(z,t)} \quad (7)$$

The remaining CH_4 is emitted to the surface with three different transport processes. First, gaseous and aqueous diffusion (F_D) occur due to concentration gradients of CH_4 ($\partial C_M(z,t)/\partial t$) (Eq. 8). The molecular diffusion coefficient (D) in different soil layers depends on soil texture and soil moisture. Ebullition (R_E) occurs when CH_4 bubble forms with C_M greater than μmol L^{-1}, and is calculated with a constant rate of K_e (1.0 h^{-1}) (Eq. 9). Plant-mediated transport (R_p) occurs for plants that function as a direct conduit for CH_4 to the atmosphere, and is functions of rate constant of 0.01 h^{-1}, vegetation type, root density, vegetation growth, and soil CH_4 concentrations (K_p, TR_{veg}, f_{ROOT}, f_{GROW}, and C_M, respectively) (Eq. 10)[68]. R_p depends on ecosystem-specific plant functional types and increases in a warmer soil due to the increase in vegetation growth. In TEM model, the soil profile was divided into 1-cm layers, and soil temperature, moisture, and CH_4 dynamics of TEM were simulated at an hourly time step[24,27].

$$F_D(z,t) = -D(z)\frac{\partial C_M(z,t)}{\partial t} \quad (8)$$

$$R_E(z,t) = K_e f(C_M(z,t)) \quad (9)$$

$$R_P(z,t) = K_P TR_{veg} f_{ROOT}(z) f_{GROW}(t) C_M(z,t) \quad (10)$$

Methane stable carbon isotope module in TEM (isoTEM). IsoTEM explicitly considers carbon isotopic fractionation processes for precursor organic matter (POM) and CH_4 during production, oxidation, and transport process. The δ^{13}C of POM (δ^{13}C-POM) is determined by the global C_3 and C_4 vegetation distribution[29] and is set to −27‰ and −13‰ for C_3- and C_4-only vegetation areas, respectively. The δ^{13}C-POM for areas with mixed C_3 and C_4 vegetation is determined by the proportion of each type of photosynthetic pathway (Supplementary Fig. 1). We also incorporated long-term trends of atmospheric δ^{13}C-CO_2 into soil δ^{13}C-POM changes. Atmospheric δ^{13}C-CO_2 became depleted in ^{13}C by ≈2‰ during 1951–2016[5,33], and this signal is transferred to photosynthates and POM for CH_4 emissions in wetlands[69]. We incorporated this trend with a 6-year carbon residence time between photosynthesis and CH_4 emission in wetlands (Supplementary Fig. 2)[31].

The CH_4 is then produced in anaerobic soils by two distinct methanogen communities: hydrogenotrophic methanogens (HMs) use H_2 and CO_2 and

acetoclastic methanogens (AMs) use acetate (CH_3COO^-) for CH_4 production[34]. Both mechanisms produce equimolar amounts of CO_2 and CH_4 from cellulose-like substrates. Using in situ observations from Holmes et al.[19] the fractional contribution of the two methanogen communities is calculated based on a multiple regression analysis with the main environmental factors (Eq. 11). From the principal component analysis, Holmes et al.[19] found a combination of environmental parameters including pH, vegetation type, soil organic carbon (SOC), and latitude are correlated with the dominant methanogenic pathway. The regression results show that fractional contribution of HMs (f_{HM}) is positively correlated with latitude with a steep increase at 60°N (slope of 0.11 and 5.19 for latitudes below and above 60°N, respectively), and negatively correlated with pH (slope of −9.23) and SOC (slope of −0.7) (R^2 of 0.41, $p < 0.001$) (Eq. 11, Supplementary Table 1, and Supplementary Fig. 3).

$$f_{HM} = \begin{cases} a_1 \times lat + b \times pH + c \times SOC + d \\ \cdots for\ latitude < latitude_{step} \\ a_1 \times lat + a_2 \times (latitude - latitude_{step}) + b \times pH + c \times SOC + d \\ \cdots for\ latitude > latitude_{step} \end{cases} \quad (11)$$

The δ^{13}C-CH_4 produced by HMs and AMs more negative than the δ^{13}C-POM, with the fractionation factors for HMs (α_{HM}) ≈ 1.030–1.080 and for AMs (α_{AM}) ≈ 1.000–1.040 (Eq. 12). The produced δ^{13}C-CH_4 is calculated using a binary mixing of CH_4 pools from the two methanogen communities (Eqs. 13, 14).

$$\alpha_{HM} = \frac{1000 + \delta^{13}C_{POM}}{1000 + \delta^{13}CH_{4,prod,HM}}, \alpha_{AM} = \frac{1000 + \delta^{13}C_{POM}}{1000 + \delta^{13}CH_{4,prod,AM}} \quad (12)$$

$$\delta^{13}CH_{4,prod,HM} = \delta^{13}C_{POM} - 1000 \times ln(\alpha_{HM}), \delta^{13}CH_{4,prod,AM} = \delta^{13}C_{POM} - 1000 \times \ln(\alpha_{AM}) \quad (13)$$

$$\delta^{13}CH_{4,prod} = f_{HM} \times \delta^{13}CH_{4,prod,HM} + (1 - f_{HM}) \times \delta^{13}CH_{4,prod,AM} \quad (14)$$

The produced CH_4 is partly oxidized by methanotrophs in aerobic soils, which prefer $^{12}CH_4$, thus α for CH_4 oxidation (α_{MO}) ≈ 1.015–1.035 (Eq. 15). Then, the produced CH_4 is transported to the atmosphere through three processes, plant-mediated transport, diffusion, and ebullition, with different fractionation factors α_{TP} ≈ 1.000–1.030, α_{TD} ≈ 1.000–1.010, α_{TE} ≈ 1.000–1.005, respectively[20] (Eq. 16).

$$\alpha_{MO} = \frac{1000 + \delta^{13}CH_{4,prod}}{1000 + \delta^{13}CH_{4,oxid}} \quad (15)$$

$$\alpha_{TP} = \frac{1000 + \delta^{13}CH_{4,prod}}{1000 + \delta^{13}CH_{4,TP}}, \alpha_{TE} = \frac{1000 + \delta^{13}CH_{4,prod}}{1000 + \delta^{13}CH_{4,TE}}, \alpha_{TD} = \frac{1000 + \delta^{13}CH_{4,prod}}{1000 + \delta^{13}CH_{4,TD}} \quad (16)$$

We calculated the oxidized and transported δ^{13}C-CH_4 based on "open system equations" at steady state to consider residual enriched CH_4 after oxidation and transport processes[70–73]. We approximated that CH_4 produced in the entire vertical soil column is either oxidized or transported in each hourly time step (Eq. 17). In Eqs. 17, 18, $M_P(z,t)$, $M_o(z,t)$, $R_P(z,t)$, and $R_E(z,t)$ represent CH_4 production, oxidation, plant-mediated transport, and ebullition rates, respectively, and $\partial F_D(z,t)/\partial z$ represents flux divergence due to gaseous and aqueous diffusion for each soil layer z and time t. For simplicity, we defined effective transport fractionation, α_T, by flux-weighting the proportions of fractionation factors of three transport processes in Eq. 19. The isotopic difference between oxidation and transport processes can be described by a fractionation factor, $\alpha_{T/MO}$, in Eq. 20. Given these conditions, isotopic signatures for oxidation and transport to the atmosphere (emission) can be written in Eqs. 21, 22. For more details, refer to Hayes[74].

$$\sum_z M_P(z,t) = \sum_z M_o(z,t) + \sum_z \frac{\partial F_D(z,t)}{\partial z} + \sum_z R_P(z,t) + \sum_z R_E(z,t) \quad (17)$$

$$f_{ox} = \frac{\sum_z M_O(z,t)}{\sum_z M_P(z,t)}, f_{TP} = \frac{\sum_z R_P(z,t)}{\sum_z M_P(z,t)}, f_{TE} = \frac{\sum_z R_E(z,t)}{\sum_z M_P(z,t)}, f_{TD} = \frac{\sum_z \frac{\partial F_D(z,t)}{\partial z}}{\sum_z M_P(z,t)} \quad (18)$$

$$\alpha_T = \frac{(f_{TP}\alpha_{TP} + f_{TE}\alpha_{TE} + f_{TD}\alpha_{TD})}{f_{TP} + f_{TE} + f_{TD}} \quad (19)$$

$$\alpha_{T/MO} = \frac{\alpha_{MO}}{\alpha_T} = \epsilon_{T/MO} + 1 \quad (20)$$

$$\delta^{13}CH_{4,oxid} = \frac{\delta^{13}CH_{4,prod} - (1 - f_{ox})\epsilon_{T/MO}}{\alpha_{T/MO}(1 - f_{ox}) + f_{ox}} \quad (21)$$

$$\delta^{13}CH_{4,emitted} = \frac{\alpha_{T/MO}\delta^{13}CH_{4,prod} + f_{ox}\epsilon_{T/MO}}{\alpha_{T/MO}(1 - f_{ox}) + f_{ox}} \quad (22)$$

Model optimization. We optimized 4 fractionation factors, α_{HM}, α_{AM}, α_{MO}, and α_{TP}, using in situ observations for six wetland ecosystem types (Eqs. 12, 15, 16). Since the fractionation factors for ebullition and diffusion are governed by physical processes, we set them as constants based on literature ($\alpha_{TE} = 1.000$, $\alpha_{TD} = 1.005$)[20]. The wetland ecosystems are divided into forested and non-forested wetlands for boreal (50–90°N), temperate (30–50°N/S), and tropical (<30°N/S) regions. To optimize parameters, we collected observation data from six sites representing each ecosystem (Supplementary Tables 2–4)[35,37,38]. For tropical wetlands, we used observation data from Burke et al.[38,75]. For forested wetlands, we used data from "Willow Marsh Trail" station, a swamp wetland dominated by hardwoods and *Lemnaceae*. For non-forested wetlands, we used data from "St. Petersburg" site where Sawgrass is the dominant vegetation. For temperate wetlands, we used data from Kelly et al.[37]. For forested wetlands, we used data from "S2 Bog" where is entirely forested with *Picea mariana*. For non-forested wetlands, we used data from "Junction Fen" where is treeless and dominated by *Carex oligosperma*. For Arctic wetlands, we used data from McCalley et al.[35]. For forested wetlands, we could not find δ^{13}C-CH_4 data from the well-drained "Palsa" occupied by woody plants, mosses, and ericaceous. Thus, we used δ^{13}C-CH_4 data from "Sphagnum" site that is in the transition between the Palsa and Eriophorum sites, and showed similar CH_4 fluxes as the "Palsa" site. For non-forested wetlands, we used data from the "Eriophorum" site.

Besides the observed meteorology from field sites, we also used CRU time-series version 4.01 to fill missing meteorological inputs[76]. We then used the Shuffled Complex Evolution Approach in R language (SCE-UA-R) to minimize the difference between simulated and observed δ^{13}C-CH_4[77]. For each site, 20 ensembles were run using SCE-UA-R with 10,000 maximum loops per parameter ensemble, and all of them reached steady state before the end of the loops. Our optimization results show that isoTEM captures the magnitude and seasonality of observed soil CH_4 fluxes and δ^{13}C-CH_4 (Supplementary Fig. 4).

Simulation setup. To estimate spatially- and temporally-varying δ^{13}C-CH_4 from global wetlands, we used spatially explicit data of land cover, soil pH and textures, meteorology and leaf area index (LAI)[24,27]. Land cover, soil pH and textures were used to assign vegetation-specific and texture-specific parameters to a grid cell[78–80]. Meteorological inputs were derived from historical air temperature, precipitation, vapor pressure, and cloudiness from gridded CRU time-series version 4.01[76]. We used monthly LAI derived from satellite imagery[81] to prescribe LAI for each 0.5° × 0.5° grid cell. All other parameters except fractionation factors were set the same as in Liu et al.[27]. We simulated global wetland CH_4 fluxes and their isotopic ratios between 1984 and 2016 at a spatial resolution of 0.5° × 0.5° with a 50-year spin-up to let the carbon isotopic composition of carbon pools come to a steady state.

Because various wetland inundation data exist[82], we first assumed that every global land grid cell can potentially be saturated, thus this product can be used with any wetland inundation data in future studies. To fill the grid cells without wetland types, we set forested and non-forested wetlands based on global vegetation types (Supplementary Fig. 5). In our analyses, simulated ecosystem-specific δ^{13}C-CH_4 from wetlands was flux weighted for each grid cell, based on CH_4 emissions simulated by TEM defined over the static inundation data from Matthews and Fung (Supplementary Fig. 6a)[49].

Model-data comparison

Site level. We compared our model results with previously published data from 58 in situ measurements compiled by Holmes et al.[19] and 66 in situ measurements by Sherwood et al.[13]. Holmes et al.[19] compiled latitude, fraction of HM and AM, pH, vegetation, and δ^{13}C-CH_4 to understand factors affecting the methanogenic pathway in global wetlands. The wetland database of Sherwood et al.[13] includes literature reference, latitude, wetland types, and measurement methods. After combining overlapped data of Holmes et al.[19] and Sherwood et al.[13] and excluding data that we used for our model optimization[35,37,38], 70 sites remained for site-level validation (Supplementary Fig. 11 and Supplementary Data 1). Due to a possible mismatch of soil and vegetation properties, and wetland distribution of grid cells between model and observation, we compared observed δ^{13}C-CH_4 with simulated δ^{13}C-CH_4 of the sampling year within two adjacent grid cells (1° × 1°) of the observation.

Regional level. We used aircraft air samples from 3 regions in Alaska from the Carbon in Arctic Reservoirs Vulnerability Experiment (CARVE)[83,84]. From 2012 to 2015, CARVE collected airborne measurements of atmospheric chemical components and relevant land surface parameters in the Alaskan Arctic to provide insights into Arctic carbon cycling. During the flights, flask-air samples were collected then sent to NOAA GML for measurements of 50 trace gases including CO_2, CH_4, CO, OCS, NMHCs, and then sent to INSTAAR for and the isotopic composition of CO_2 and CH_4. After excluding airborne data with flags, there are 1476 measurements during the sampling period.

In situ flux observations collected across Alaskan wetlands show an average of −65‰ but a large 9‰ variation, due to the complex vegetation and soil properties[40]. To compare the spatial variability of wetland δ^{13}C-CH_4, we divided the Alaskan continent into three regions: North Slope, interior, and southwest Alaska based on latitude (62–68 °N, 52–62 °N and 140–155 °W, and 52–62 °N and 155–170 °W for North Slope, interior, and southwest Alaska, respectively). We used Miller-Tans plots to identify the source signatures of δ^{13}C-CH_4 from wetlands using the airborne measurements[39]. To identify wetland isotopic signatures, we removed measurements that may have effects from fossil fuel emission (C_3H_8 < 300 ppt), biomass burning (CO < 300 ppb), and transport influence (Altitude < 1500 m), and we set the background altitude to >5000 m. After plotting the data, 2014 was excluded due to limited data and small R^2 (Supplementary Table 5).

Uncertainty and sensitivity tests

Long-term trends in wetland δ^{13}C-CH_4 from observations. We considered latitude, pH, and soil carbon as key parameters that determine variability of wetland δ^{13}C-CH_4 to run a linear regression using the site-level observations collected from global wetlands since the early 1980s (Supplementary Data 1). We added year as additional parameter for the linear regression and see if it improves the fit with data. The regression results show that wetland δ^{13}C-CH_4 is negatively correlated with year, latitude, and SOC (slope of −0.11, −0.10, and −0.20, respectively), and positively correlated with pH (slope of 2.21) (R^2 of 0.30, $p < 0.001$) (Eq. 23, Supplementary Fig. 17, and Supplementary Table 6). The regression without year as a parameter showed smaller coefficient (R^2 of 0.25, $p < 0.001$).

$$\delta^{13}C - CH_4 = a \times lat + b \times pH + c \times SOC + d \times year + e \quad (23)$$

Markov Chain Monte Carlo for the fraction of HM (f_{HM}). We used a Markov Chain Monte Carlo (MCMC) approach for parameter uncertainty estimation for f_{HM}. MCMC is a method for estimating the posterior probability density function for asset of parameters, given priors on those parameters and a set of observations[45]. We used independent, uniform prior probability density functions for each parameter in Supplementary Table 1. Thirty-nine data points from Holmes et al.[19] were used to constrain the model. Gaussian errors were assumed. We generated a Markov chain with 100,000 elements to estimate the joint posterior probability density functions. The chain converged after about 10,000 elements. We used the posterior probability density function to estimate the uncertainty of parameter (Supplementary Table 1).

Sensitivity test with meteorological and substrate inputs, f_{HM}, and inundation. We conducted 8 sensitivity tests of meteorology and substrate inputs. Specifically, we altered air temperature by ±3 °C, precipitation by ±30%, and atmospheric CH_4 abundance by ±30%, and NPP by ±30%, uniformly for each grid cell, while maintaining all other variables at their default isoTEM values. We also varied parameters for f_{HM} based on the uncertainty range from MCMC (Supplementary Table 1). We further varied a wetland inundation using satellite-driven Surface WAter Microwave Product Series-Global Lakes and Wetlands Database (SWAMPS-GLWD)[48].

Forward modeling using TM5 atmospheric model

Global mass balance for bottom-up inventory. We adjusted global long-term mean fossil fluxes to match the simulated growth rate of CH_4 during 1984–2016 and the 1998–2016 mean of δ^{13}C-CH_4 with observation (Table 1 and Supplementary Table 11). Lan et al.[26] showed that there is an offset of simulated global mean δ^{13}C-CH_4 when using EDGAR 4.3.2 inventory as the inventory underestimates fossil fluxes. To remove the offset and compare our scenarios fairly, we adjusted fossil fluxes between 170 and 190 $TgCH_4yr^{-1}$ (Supplementary Fig. 19), within the uncertainty range in Schwietzke et al.[9]. To satisfy the global mass balance, we ran one box model that included CH_4 sources of biogenic, fossil and biomass/biofuel emissions, with corresponding isotopic signatures, and CH_4 sinks due to reaction with OH, Cl, and $O(^1D)$ and soil bacteria, all with different fractionation factor. When we increased or decreased fossil fluxes, we accordingly decreased or increased ruminant flux, respectively, so the total annual CH_4 fluxes followed the observed atmospheric CH_4 growth rate, and the long-term mean total emission was set to 536–538 $TgCH_4yr^{-1}$ during 1984–2016. For more details on the setup and equations for global mass balance, refer to Lan et al.[26].

Data sources for CH_4 emissions and its isotopic source signatures. We used the bottom-up inventory constructed by Lan et al.[26] (Supplementary Table 8). In specific, for CH_4 emissions, we used GFED 4.1 s for biomass burning for 1997–2016[85] and annual emissions from the Reanalysis of Tropospheric chemical composition project before 1997, and the EDGAR 4.3.2 inventory for other anthropogenic emissions for 1984–2016[86]. For emissions from geological seeps, we used gridded emission from Etiope et al.[87]. Emission estimates from wild animals and termites were adopted from Bergamaschi et al.[88]. For δ^{13}C-CH_4 source signature, fossil fuel source signature data were based on the global δ^{13}C-CH_4 source signature inventory 2020[89], where the data were categorized by coal gas, conventional gas, and shale gas. Biomass burning, biofuel burning, ruminant, and wild animal δ^{13}C-CH_4 data were based on the global maps of C_3/C_4 distribution[29]. The geological seeps δ^{13}C-CH_4 data were from Etiope et al.[87].

TM5 atmospheric modeling of CH_4 and δ^{13}C-CH_4. Atmospheric CH_4 mole fractions and δ^{13}C-CH_4 were simulated from 1984 to 2016 by coupling the surface fluxes and isotope source signatures from the bottom-up inventory with the TM5 tracer transport model driven by ECMWF ERA Interim meteorology with the 4DVAR branch of the TM5 model[90,91]. TM5 was run globally at 6° × 4° over 25 vertical sigma-pressure hybrid levels, for total CH_4 and ^{13}C-CH_4. For each source type, ^{13}C-CH_4 fluxes were derived from total CH_4 fluxes and source-specific isotope source signatures. We spun up our model during 1984–1999 and selected 2000–2016 to compare with atmospheric observations to ensure our spin-up period was sufficient for equilibration of atmospheric δ^{13}C-CH_4 inter-hemispheric gradient[26,92]. As per Lan et al.[26] we applied tropospheric Cl sink of Hossaini et al.[51] and the OH field from Spivakovsky et al.[14] with a fractionation factor of −3.9‰. The CH_4 sinks varied spatially and seasonally but did not change interannually. For more details on setup for TM5 modeling, refer to Lan et al.[26].

Atmospheric CH_4 and δ^{13}C-CH_4 measurement. Observational data of atmospheric CH_4 and δ^{13}C-CH_4 used to evaluate model results are from flask-air measurements from NOAA's Global Greenhouse Gas Reference Network[26,54]. The flask-air samples was analyzed for δ^{13}C-CH_4 at the Institute of Arctic and Alpine Research (INSTAAR), University of Colorado, Boulder. Gas chromatography-Isotope-ratio mass spectrometry (GC-IRMS) is used for δ^{13}C-CH_4 analysis[5]. The δ^{13}C-CH_4 in air measurements are referenced against the Vienna Pee Dee Belemnite (VPDB) standard (Eq. 1). A subset of the observation sites predominantly influenced by well-mixed background air is used to construct a Marine Boundary Layer (MBL) zonally averaged surface using methods developed by Masarie and Tans (1995)[93], to represent the observational-based global long-term trend and north–south gradient. This includes 31 sites with CH_4 measurements during study period of 1984–2016 and 10 of which with δ^{13}C-CH_4 measurements staring in 1998 (Supplementary Fig. 21 and Supplementary Table 10). More details on the MBL data products and uncertainties can be found at https://www.esrl.noaa.gov/gmd/ccgg/mbl/mbl.html. For model-observation comparisons, model results from the same set of MBL sites are sampled, and the same calculation methods are applied to model results and observations for global long-term and north–south gradient. The north–south gradient was calculated as the difference of atmospheric δ^{13}C-CH_4 between 60–90 °S and 60–90 °N.

Atmospheric modeling with transient inundation data for Scenarios E-H. Since we used static wetland inundation data[49] for our default Scenarios A–D, we used transient wetland inundation data from Poulter et al.[48] and ran TM5 atmospheric model (Supplementary Figs. 26–30 and Supplementary Table 11). Same as Scenarios A–C, we constructed Scenarios E–G with different wetland isotopic signature maps as inputs for TM5 atmospheric modeling in 1984–2016. In specific, the first uses a globally uniform wetland δ^{13}C-CH_4 of −62.3‰, the mean wetland signature from Ganesan et al.[23] (referred to as Scenario E), the other uses a static wetland isotope spatial map from Ganesan et al.[23] (referred to as Scenario F), and the last used spatially- and temporally-resolved maps from isoTEM (referred to as Scenario G).

The wetland fluxes for Scenarios E–G are based on Liu et al.[27] and transient inundation[48] but applied an increase in fluxes after 2006 by hypothesizing that the microbial wetland emission is a dominant driver of post-2006 atmospheric CH_4 increase (Supplementary Fig. 26), same as Scenarios A–C. We also conducted the global mass balance by adjusting global long-term mean fossil fluxes between 160 and 180 $TgCH_4yr^{-1}$ for Scenarios E–G to match the simulated growth rate of CH_4 during 1984–2016 and the 1998–2016 mean of annual δ^{13}C-CH_4 with observations.

Scenarios E–G reproduced the observed global CH_4 growth rate during 1984–2016 and the global long-term mean δ^{13}C-CH_4 with observation during 1998–2016 (Supplementary Fig. 28), as we set the fluxes based on the mass balance. However, Scenarios E–G with transient inundation data underestimated the north–south δ^{13}C-CH_4 gradient (0.27 ± 0.06‰) compared with observations (0.45 ± 0.05‰) (Supplementary Fig. 29). Thus, we ran an additional scenario H that increased emissions from boreal wetlands by 2.5 times over the original transient data (Supplementary Fig. 26 and Supplementary Table 11), which improved the match with the observed north–south δ^{13}C-CH_4 gradient (0.39‰) (Supplementary Fig. 29). The site-level comparison with atmospheric δ^{13}C-CH_4 from 10 observation sites also confirmed that Scenario H more closely reproduced the observation (Supplementary Fig. 30). This implies that the transient inundation data from Poulter et al.[48] may need more wetland emissions from boreal regions as found in static inundation data[49] (Supplementary Fig. 6) and other satellite-derived inundation data[94].

Data availability

Supplementary Data 1 is available at: https://figshare.com/articles/dataset/Supplementary_Data_1_of_Oh_et_al_2022_/19929965. The stable carbon isotopic composition of wetland emissions is available at: https://doi.org/10.25925/9s6n-g811.

Code availability

The code is also archived and available at: https://doi.org/10.15138/cem6-ka15.

Received: 9 November 2021; Accepted: 22 June 2022;
Published online: 12 July 2022

References

1. Etheridge, D. M., Steele, L., Francey, R. J. & Langenfelds, R. L. Atmospheric methane between 1000 AD and present: Evidence of anthropogenic emissions and climatic variability. *J. Geophys. Res. Atmos.* **103**, 15979–15993 (1998).
2. Dlugokencky, E.J., Crotwell, A.M., Mund, J.W., Crotwell, M.J. & Thoning, K.W. NOAA global greenhouse gas reference network flask-air sample measurements of CO_2, CH_4, CO, N_2O, H_2, SF_6 and isotopic ratios at global and regional background sites, 1967—Present. https://doi.org/10.15138/VNCZ-M766 (2022).
3. Dlugokencky, E. J., Nisbet, E. G., Fisher, R. & Lowry, D. Global atmospheric methane: budget, changes and dangers. *Philos. Trans. R. Soc. A Math. Phys. Eng. Sci.* **369**, 2058–2072 (2011).
4. Ferretti, D. F. et al. Atmospheric science: unexpected changes to the global methane budget over the past 2000 years. *Science* **309**, 1714–1717 (2005).
5. White, J.W.C., Vaughn, B. H. & Michel, S. E. University of Colorado, Institute of Arctic and Alpine Research (INSTAAR), Stable Isotopic Composition of Atmospheric Methane (^{13}C) from the NOAA ESRL Carbon Cycle Cooperative Global Air Sampling Network, 1998–2017, Version: 2018-09-24. ftp://aftp.cmdl.noaa.gov/data/trace_gases/ch4c13/flask/ (2018).
6. Hausmann, P., Sussmann, R. & Smale, D. Contribution of oil and natural gas production to renewed increase in atmospheric methane (2007–2014): top–down estimate from ethane and methane column observations. *Atmos. Chem. Phys.* **16**, 3227–3244 (2016).
7. Naus, S. et al. Constraints and biases in a tropospheric two-box model of OH. *Atmos. Chem. Phys.* **19**, 407–424 (2019).
8. Schaefer, H. et al. A 21st-century shift from fossil-fuel to biogenic methane emissions indicated by 13CH4. *Science* **352**, 80–84 (2016).
9. Schwietzke, S. et al. Upward revision of global fossil fuel methane emissions based on isotope database. *Nature* **538**, 88–91 (2016).
10. Worden, J. R. et al. Reduced biomass burning emissions reconcile conflicting estimates of the post-2006 atmospheric methane budget. *Nat. Commun.* **8**, 1–11 (2017).
11. Turner, A. J., Frankenberg, C. & Kort, E. A. Interpreting contemporary trends in atmospheric methane. *Proc. Natl. Acad. Sci.* **116**, 2805–2813 (2019).
12. Saunois, M. et al. The global methane budget 2000–2017. *Earth system science data*, **12**, 1561–1623 (2020).
13. Sherwood, O. A., Schwietzke, S., Arling, V. A. & Etiope, G. Global inventory of gas geochemistry data from fossil fuel, microbial and burning sources, version 2017. *Earth Syst. Sci. Data* **9**, 639–656 (2017).
14. Spivakovsky, C. M. et al. Three-dimensional climatological distribution of tropospheric OH: Update and evaluation. *J. Geophys. Res. Atmos.* **105**, 8931–8980 (2000).
15. Strode, S. A. et al. Strong sensitivity of the isotopic composition of methane to the plausible range of tropospheric chlorine. *Atmos. Chem. Phys.* **20**, 8405–8419 (2020).
16. Rice, A. L. et al. Atmospheric methane isotopic record favors fossil sources flat in 1980s and 1990s with recent increase. *Proc. Natl. Acad. Sci.* **113**, 10791–10796 (2016).
17. Feinberg, A. I., Coulon, A., Stenke, A., Schwietzke, S. & Peter, T. Isotopic source signatures: Impact of regional variability on the $\delta^{13}CH_4$ trend and spatial distribution. *Atmos. Environ.* **174**, 99–111 (2018).
18. Brownlow, R. et al. Isotopic ratios of tropical methane emissions by atmospheric measurement. *Global Biogeochem. Cycles* **31**, 1408–1419 (2017).
19. Holmes, M. E., Chanton, J. P., Tfaily, M. M. & Ogram, A. CO_2 and CH_4 isotope compositions and production pathways in a tropical peatland. *Global Biogeochem. Cycles* **29**, 1–18 (2015).
20. Chanton, J. P. The effect of gas transport on the isotope signature of methane in wetlands. *Org. Geochem.* **36**, 753–768 (2005).
21. Fisher, R. E. et al. Measurement of the ^{13}C isotopic signature of methane emissions from northern European wetlands. *Global Biogeochem. Cycles* **31**, 605–623 (2017).
22. Nakagawa, F., Yoshida, N., Nojiri, Y. & Makarov, V. Production of methane from alasses in eastern Siberia: Implications from its ^{14}C and stable isotopic compositions. *Global Biogeochem. Cycles* **16**, 14-1–14-15 (2002).
23. Ganesan, A. L. et al. Spatially resolved isotopic source signatures of wetland methane emissions. *Geophys. Res. Lett.* **45**, 3737–3745 (2018).
24. Zhuang, Q. et al. Methane fluxes between terrestrial ecosystems and the atmosphere at northern high latitudes during the past century: a retrospective analysis with a process-based biogeochemistry model. *Global Biogeochem. Cycles* **18**, GB3010 (2004).
25. Oh, Y. et al. Reduced net methane emissions due to microbial methane oxidation in a warmer Arctic. *Nat. Clim. Chang.* **10**, 317–321 (2020).
26. Lan, X. et al. Improved constraints on global methane emissions and sinks using $\delta^{13}C$-CH_4. *Global Biogeochem. Cycles* https://doi.org/10.1029/2021gb007000 (2021).
27. Liu, L. et al. Uncertainty quantification of global net methane emissions from terrestrial ecosystems using a mechanistically-based biogeochemistry model. *J. Geophys. Res. Biogeosci.* **125**, e2019JG005428 (2020).
28. Zhuang, Q. et al. Response of global soil consumption of atmospheric methane to changes in atmospheric climate and nitrogen deposition. *Global Biogeochem. Cycles* **27**, 650–663 (2013).
29. Still, C. J., Berry, J. A., Collatz, G. J. & DeFries, R. S. Global distribution of C_3 and C_4 vegetation: Carbon cycle implications. *Global Biogeochem. Cycles* **17**, 6-1–61-4 (2003).
30. Holmes, M. E., Chanton, J. P., Bae, H. S. & Ogram, A. Effect of nutrient enrichment on $\delta^{13}CH_4$ and the methane production pathway in the Florida Everglades. *J. Geophys. Res. Biogeosci.* **119**, 1267–1280 (2014).
31. Lassey, K. R., Etheridge, D. M., Lowe, D. C., Smith, A. M. & Ferretti, D. F. Centennial evolution of the atmospheric methane budget: What do the carbon isotopes tell us? *Atmos. Chem. Phys.* **7**, 2119–2139 (2007).
32. Keeling, R. F. et al. Atmospheric evidence for a global secular increase in carbon isotopic discrimination of land photosynthesis. *Proc. Natl. Acad. Sci. USA* **114**, 10361–10366 (2017).
33. Graven, H. et al. Compiled records of carbon isotopes in atmospheric CO_2 for historical simulations in CMIP6. *Geosci. Model Dev.* **10**, 4405–4417 (2017).
34. Horn, M. A., Matthies, C., Küsel, K., Schramm, A. & Drake, H. L. Hydrogenotrophic methanogenesis by moderately acid-tolerant methanogens of a methane-emitting acidic peat. *Appl. Environ. Microbiol.* **69**, 74–83 (2003).
35. McCalley, C. K. et al. Methane dynamics regulated by microbial community response to permafrost thaw. *Nature* **514**, 478–481 (2014).
36. Le Mer, J. & Roger, P. Production, oxidation, emission and consumption of methane by soils: a review. *Eur. J. Soil Biol.* **37**, 25–50 (2001).
37. Kelly, C. A., Carolina, N., Hill, C., Dise, B. & Martens, C. S. Temporal variations in the stable carbon isotopic composition of methane emitted from Minnesota peatlands. *Global Biogeochem. Cycles* **6**, 263–269 (1992).
38. Burke, R. A., Barber, T. R. & Sackett, W. M. Methane flux and stable hydrogen and carbon isotope composition of sedimentary methane from the Florida Everglades. *Global Biogeochem. Cycles* **2**, 329–340 (1988).
39. Miller, J. B. & Tans, P. P. Calculating isotopic fractionation from atmospheric measurements at various scales. *Tellus Ser. B Chem. Phys. Meteorol.* **55**, 207–214 (2003).
40. Chanton, J. P., Fields, D. & Hines, M. E. Controls on the hydrogen isotopic composition of biogenic methane from high-latitude terrestrial wetlands. *J. Geophys. Res. Biogeosci.* **111**, 1–9 (2006).
41. Tang, J., Zhuang, Q., Shannon, R. D. & White, J. R. Quantifying wetland methane emissions with process-based models of different complexities. *Biogeosciences* **7**, 3817–3837 (2010).
42. Zhu, X. et al. Rising methane emissions in response to climate change in Northern Eurasia during the 21st century. *Environ. Res. Lett.* **6**, 45211 (2011).
43. Lu, X. & Zhuang, Q. Modeling methane emissions from the Alaskan Yukon River basin, 1986–2005, by coupling a large-scale hydrological model and a process-based methane model. *J. Geophys. Res. Biogeosci.* **117**, G2 (2012).
44. Jin, Z., Zhuang, Q., He, J.-S., Zhu, X. & Song, W. Net exchanges of methane and carbon dioxide on the Qinghai-Tibetan Plateau from 1979 to 2100. *Environ. Res. Lett.* **10**, 85007 (2015).
45. Gilks, W. R., Richardson, S. & Spiegelhalter, D. *Markov chain Monte Carlo in practice*. (CRC press, 1995).
46. Conrad, R. Quantification of methanogenic pathways using stable carbon isotopic signatures: A review and a proposal. *Org. Geochem.* **36**, 739–752 (2005).
47. Blaser, M. & Conrad, R. Stable carbon isotope fractionation as tracer of carbon cycling in anoxic soil ecosystems. *Curr. Opin. Biotechnol.* **41**, 122–129 (2016).
48. Poulter, B. et al. Global wetland contribution to 2000–2012 atmospheric methane growth rate dynamics. *Environ. Res. Lett.* **12**, 094013 (2017).
49. Matthews, E. & Fung, I. Methane emission from natural wetlands: Global distribution, area, and environmental characteristics of sources. *Global Biogeochem. Cycles* **1**, 61–86 (1987).
50. Nisbet, E. G., Dlugokencky, E. J. & Bousquet, P. Methane on the rise—again. *Science* **343**, 493–495 (2014).
51. Hossaini, R. et al. A global model of tropospheric chlorine chemistry: Organic versus inorganic sources and impact on methane oxidation. *J. Geophys. Res. Atmos.* **121**, 14–271 (2016).
52. Saueressig, G. et al. Carbon 13 and D kinetic isotope effects in the reactions of CH_4 with O (^1D) and OH: new laboratory measurements and their implications for the isotopic composition of stratospheric methane. *J. Geophys. Res. Atmos.* **106**, 23127–23138 (2001).
53. Stein, T. Increase in atmospheric methane set another record during 2021. *NOAA Res. News* (2022).
54. Dlugokencky, E. Trends in atmopsheric methane. *NOAA/ESRL* https://gml.noaa.gov/ccgg/trends_ch4/ (2022).

55. Stein, T. New analysis shows microbial sources fueling rise of atmospheric methane. *NOAA Research News*. https://research.noaa.gov/article/ArtMID/587/ArticleID/2769/New-analysis-shows-microbial-sources-fueling-rise-of-atmospheric-methane (2021).
56. Nisbet, E. G. et al. Very strong atmospheric methane growth in the 4 years 2014–2017: implications for the paris agreement. *Global Biogeochem. Cycles* **33**, 318–342 (2019).
57. Qiu, C. et al. A strong mitigation scenario maintains climate neutrality of northern peatlands. *One Earth* **5**, 86–97 (2022).
58. Schuur, E. A. G. et al. The effect of permafrost thaw on old carbon release and net carbon exchange from tundra. *Nature* **459**, 556–559 (2009).
59. Sullivan, T. D. et al. Influence of permafrost thaw on an extreme geologic methane seep. *Permafr. Periglac. Process* **32**, 484–502 (2021).
60. Walter Anthony, K. M., Anthony, P., Grosse, G. & Chanton, J. Geologic methane seeps along boundaries of Arctic permafrost thaw and melting glaciers. *Nat. Geosci.* **5**, 419–426 (2012).
61. Corbett, J. E. et al. Partitioning pathways of CO_2 production in peatlands with stable carbon isotopes. *Biogeochemistry* **114**, 327–340 (2013).
62. Deng, J. et al. Adding stable carbon isotopes improves model representation of the role of microbial communities in peatland methane cycling. *J. Adv. Model. Earth Syst.* **9**, 1412–1430 (2017).
63. Hodgkins, S. B. et al. Changes in peat chemistry associated with permafrost thaw increase greenhouse gas production. *Proc. Natl. Acad. Sci. USA* **111**, 5819–5824 (2014).
64. Pangala, S. R. et al. Large emissions from floodplain trees close the Amazon methane budget. *Nature* **552**, 230–234 (2017).
65. Barba, J. et al. Methane emissions from tree stems: a new frontier in the global carbon cycle. *New Phytol.* **222**, 18–28 (2019).
66. Rosentreter, J. A. et al. Half of global methane emissions come from highly variable aquatic ecosystem sources. *Nat. Geosci.* **14**, 225–230 (2021).
67. Zhuang, Q. et al. Modeling soil thermal and carbon dynamics of a fire chronosequence in interior Alaska. *J. Geophys. Res. D Atmos.* **108**, (2003).
68. Walter, B. P. & Heimann, M. A process-based, climate-sensitive model to derive methane emissions from natural wetlands: Application to five wetland sites, sensitivity to model parameters, and climate. *Global Biogeochem. Cycles* **14**, 745–765 (2000).
69. Wingate, L. et al. Photosynthetic carbon isotope discrimination and its relationship to the carbon isotope signals of stem, soil and ecosystem respiration. *New Phytol.* **188**, 576–589 (2010).
70. Monson, K. D. & Hayes, J. M. Biosynthetic control of the natural abundance of carbon 13 at specific positions within fatty acids in Escherichia coli. Evidence regarding the coupling of fatty acid and phospholipid synthesis. *J. Biol. Chem.* **255**, 11435–11441 (1980).
71. Mahieu, K., De Visscher, A., Vanrolleghem, P. A. & Van Cleemput, O. Modelling of stable isotope fractionation by methane oxidation and diffusion in landfill cover soils. *Waste Manag.* **28**, 1535–1542 (2008).
72. Preuss, I., Knoblauch, C., Gebert, J. & Pfeiffer, E. M. Improved quantification of microbial CH_4 oxidation efficiency in arctic wetland soils using carbon isotope fractionation. *Biogeosciences* **10**, 2539–2552 (2013).
73. Throckmorton, H. M. et al. Pathways and transformations of dissolved methane and dissolved inorganic carbon in Arctic tundra watersheds: Evidence from analysis of stable isotopes. *Global Biogeochem. Cycles* **29**, 1893–1910 (2015).
74. Hayes, J. M. An introduction to isotopic calculations. *Woods Hole Oceanogr. Inst.* 1–10 (2004).
75. Burke, R. A. Jr, Barber, T. R. & Sackett, W. M. Seasonal variations of stable hydrogen and carbon isotope ratios of methane in subtropical freshwater sediments. *Global Biogeochem. Cycles* **6**, 125–138 (1992).
76. Harris, I., Jones, P. D., Osborn, T. J. & Lister, D. H. Updated high-resolution grids of monthly climatic observations - the CRU TS3.10 Dataset. *Int. J. Climatol.* **34**, 623–642 (2014).
77. Duan, Q. Y., Gupta, V. K. & Sorooshian, S. Shuffled complex evolution approach for effective and efficient global minimization. *J. Optim. Theory Appl.* **76**, 501–521 (1993).
78. Melillo, J. M. et al. Global climate change and terrestrial net primary production. *Nature* **363**, 234 (1993).
79. Global Soil Data Task. 2000. Global Soil Data Products CD-ROM (IGBP-DIS). CD-ROM. International Geosphere-Biosphere Programme, Data and Information System, Potsdam, Germany. Available from Oak Ridge National Laboratory Distributed Active Archive Center, Oak Ridge, Tennessee, U.S.A. [http://www.daac.ornl.gov].
80. Zhuang, Q. et al. Carbon cycling in extratropical terrestrial ecosystems of the Northern Hemisphere during the 20th century: A modeling analysis of the influences of soil thermal dynamics. *Tellus Ser. B Chem. Phys. Meteorol.* **55**, 751–776 (2003).
81. Myneni, R. B. et al. Global products of vegetation leaf area and fraction absorbed PAR from year one of MODIS data. *Remote Sens. Environ.* **83**, 214–231 (2002).
82. Melton, J. R. et al. Present state of global wetland extent and wetland methane modelling: conclusions from a model inter-comparison project (WETCHIMP). *Biogeosciences* **10**, 753–788 (2013).
83. Miller, S. M. et al. A multiyear estimate of methane fluxes in Alaska from CARVE atmospheric observations. *Global Biogeochem. Cycles* **30**, 1441–1453 (2016).
84. Chang, R. Y. W. et al. Methane emissions from Alaska in 2012 from CARVE airborne observations. *Proc. Natl. Acad. Sci. USA* **111**, 16694–16699 (2014).
85. Werf, G. R. et al. Global fire emissions estimates during 1997–2016. *Earth Syst. Sci. Data* **9**, 697–720 (2017).
86. Janssens-Maenhout, G. et al. EDGAR v4. 3.2 Global Atlas of the three major Greenhouse Gas Emissions for the period 1970–2012. *Earth Syst. Sci. Data* **11**, 959–1002 (2019).
87. Etiope, G. & Schwietzke, S. Global geological methane emissions: an update of top-down and bottom-up estimates. *Elem. Sci. Anth.* **7**, 47 (2019).
88. Bergamaschi, P. et al. Satellite chartography of atmospheric methane from SCIAMACHY on board ENVISAT: 2. Evaluation based on inverse model simulations. *J. Geophys. Res. Atmos.* **112**, https://doi.org/10.1029/2006JD007268 (2007).
89. Sherwood, O. A. et al. Global $\delta^{13}C$-CH_4 Source Signature Inventory. https://doi.org/10.15138/qn55-e011 (2020).
90. Basu, S. et al. Global CO_2 fluxes estimated from GOSAT retrievals of total column CO_2. *Atmos. Chem. Phys. Discuss.* **13**, 8695–8717 (2013).
91. Meirink, J. F., Bergamaschi, P. & Krol, M. C. Four-dimensional variational data assimilation for inverse modelling of atmospheric methane emissions: method and comparison with synthesis inversion. *Atmos. Chem. Phys.* **8**, 6341–6353 (2008).
92. Tans, P. P. A note on isotopic ratios and the global atmospheric methane budget. *Global Biogeochem. Cycles* **11**, 77–81 (1997).
93. Masarie, K. A. & Tans, P. P. Extension and integration of atmospheric carbon dioxide data into a globally consistent measurement record. *J. Geophys. Res. Atmos.* **100**, 11593–11610 (1995).
94. Prigent, C., Jimenez, C. & Bousquet, P. Satellite-derived global surface water extent and dynamics over the last 25 years (GIEMS-2). *J. Geophys. Res. Atmos.* **125**, e2019JD030711 (2020).

Acknowledgements

This work was supported by NASA Earth and Space Science Fellowship Program (#80NSSC17K0368 P00001) and Interdisciplinary Research in Earth Science (#NNX17AK20G). We thank Carmody K. McCalley for providing data and John Mund for technical support.

Author contributions

Y.O., Q.Z., and X.L. conceived the study. Y.O., Q.Z., L.L., and L.R.W. built the model. E.J.D., S.E.M., J.B.M., S.S., and P.C. provided unpublished or raw data. Y.O. conducted model runs. S.B., L.B., P.T., and J.P.C., and all other authors contributed to data interpretation and preparation of paper text.

Competing interests

The authors declare no competing interests.

Additional information

Supplementary information The online version contains supplementary material available at https://doi.org/10.1038/s43247-022-00488-5.

Correspondence and requests for materials should be addressed to Youmi Oh or Qianlai Zhuang.

Peer review information *Communications Earth & Environment* thanks the anonymous reviewers for their contribution to the peer review of this work. Primary handling editors: Leiyi Chen and Clare Davis.